



# High-performance perovskite solar cells based on dopant-free hole-transporting material fabricated by a thermal-assisted blade-coating method with efficiency exceeding 21%

Kun-Mu Lee<sup>a,b,c</sup>, Wei-Hao Chiu<sup>c</sup>, Yu-Hsiang Tsai<sup>d</sup>, Chao-Shian Wang<sup>e</sup>, Yu-Tai Tao<sup>f</sup>, Yan-Duo Lin<sup>e,\*</sup>

<sup>a</sup> Department of Chemical and Materials Engineering, Chang Gung University, Taoyuan 33302, Taiwan

<sup>b</sup> Division of Neonatology, Department of Pediatrics, Chang Gung Memorial Hospital, Linkou Taoyuan 33305, Taiwan

<sup>c</sup> Center for Green Technology, Chang Gung University, Taoyuan 33302, Taiwan

<sup>d</sup> Department of Applied Chemistry, National Chiayi University, Chiayi 60004, Taiwan

<sup>e</sup> Department of Chemistry, Soochow University, Taipei 11102, Taiwan

<sup>f</sup> Institute of Chemistry, Academia Sinica, Taipei 115024, Taiwan

## ARTICLE INFO

### Keywords:

Dopant-free hole-transporting material  
Cyclopenta[2,1-b;3,4-b']dithiophene  
Fully printed perovskite solar cell  
Thermal-assisted blade-coating

## ABSTRACT

As the performance in terms of efficiency and device stability of perovskite solar cells (PSCs) has made rapid progress in a short period of time, the upscaling of PSCs becomes an important issue for massive commercial applications, where the cost of device manufacturing is a determining factor for wide spread uses. Device fabrication by printing technique is one such low-cost process for large scale preparation. However, one of the reasons limiting the progress of a fully printed PSCs is the lack of appropriate hole-transporting materials (HTMs) that can be printed. Herein, a new donor-acceptor-donor (D-A-D) type hole-transporting material with 4-dicyanomethylene-4H-cyclopenta[2,1-b;3,4-b']dithiophene (diCN-CPDT) core tethered with two bis(alkoxy) diphenylaminocarbazole periphery groups, namely **CB**, was synthesized and applied as dopant-free HTM in fully printed PSCs by thermal-assisted blade-coating (TABC) method. The PSCs fabricated by fully scalable processes based on dopant-free **CB** as HTM exhibited an impressive power conversion efficiency (PCE) up to 21.09%, which is higher than that of devices with doped 2,2',7,7'-tetrakis-(*N,N*-di-*p*-methoxyphenylamine)9,9'-spirobifluorene (spiro-OMeTAD) (14.28%) under the same fabricating condition. Furthermore, the all TABC process is demonstrated to produce an area of 10 cm × 10 cm for the devices except for electrode with an average PCE of 19.68%. Additionally, the TABC-based dopant-free **CB**-based PSCs exhibited significantly improved long-term stability, retaining more than 94% PCE after 500 h compared to that using doped spiro-OMeTAD under a relative humidity of ~50%. This result demonstrated that the newly developed **CB** is a promising candidate HTM for high-performance fully printable PSCs.

## 1. Introduction

Since the first report by Miyasaka and co-workers in 2009 [1], organic-inorganic hybrid halide perovskite solar cells (PSCs) have attracted widespread attention as a promising next-generation photovoltaic technology because they have advantages of low-cost fabrication and remarkable power conversion efficiencies (PCEs) [2–4]. The reported PCEs of PSCs have grown rapidly, from the initial 3.8% to a certified 25.5% over the last decade, suggesting PSCs to be ideal alternative to conventional inorganic photovoltaic devices [5]. In a typical

PSCs, the hole-transporting material (HTM) is one of the key components because it plays a significant role in extracting holes from the perovskite layer and transporting them to the electrode for effectively reducing the charge recombination processes at the perovskite/HTM interfaces, which is essential for achieving high PCEs. It can also serve as a barrier to prevent the decomposition of the perovskite due to moisture and oxygen penetration. Despite the remarkable PCEs exhibited by PSCs, there are several problems that need to be solved. In particular, the development of PSCs with long-term stability and industrially compatible deposition techniques for commercial application in the future. So

\* Corresponding author.

E-mail address: [ymlin@scu.edu.tw](mailto:ymlin@scu.edu.tw) (Y.-D. Lin).

<https://doi.org/10.1016/j.cej.2021.131609>

Received 6 May 2021; Received in revised form 24 July 2021; Accepted 27 July 2021

Available online 10 August 2021

1385-8947/© 2021 Elsevier B.V. All rights reserved.

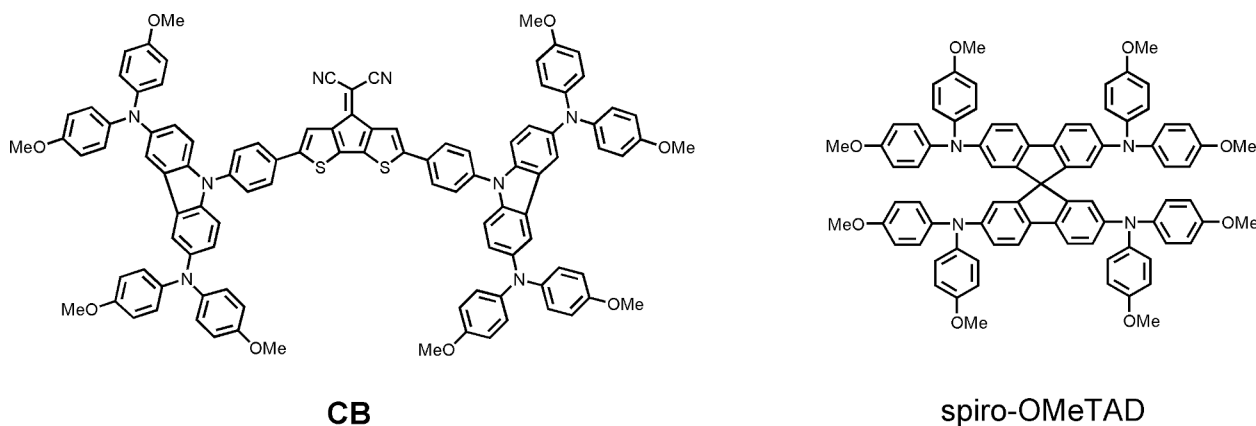


Fig. 1. Chemical structures of **CB** and spiro-OMeTAD.

far, 2,2',7,7'-tetrakis(*N,N*-di-*p*-methoxyphenyl-amine)9,9'-spirobi-fluorene (spiro-OMeTAD) is widely used as HTM for high-efficiency PSCs [6–7]. However, the synthesis of spiro-OMeTAD requires complex synthetic procedures and tedious purifications, which constitute major obstacles for commercialization [8–9]. In addition, spiro-OMeTAD in its pristine form suffers from low hole-mobility and conductivity, and therefore chemical dopants and additives such as 4-*tert*-butylpyridine (*t*-BP), lithium bis(tri-fluoromethanesulfonyl)imide (Li-TFSI) or cobalt complexes are required to improve the charge transport properties and device performances [10–11]. Unfortunately, lithium salts are hygroscopic and sensitive to the moisture, leading to degradation of perovskite layer [12–16]. In addition, *t*-BP tends to interact with  $\text{PbI}_2$  to form a new complex and therefore accelerates decomposition of perovskite materials, resulting in unstable PSCs [17–20]. Therefore, it is urgently necessary to develop dopant-free HTMs for PSCs.

Recently, considerable efforts have been devoted to the design and synthesis of new dopant-free alternative HTMs, including small molecules and conjugated polymers, for application in PSCs [21–30]. It is well known that small molecules have a number of advantages over their polymeric counterparts, including ease of synthesis and purification, good batch-to-batch reproducibility, and easy-to-tune HOMO energy levels. Although many dopant-free small-molecule-based HTMs have been explored based on different central skeletons such as benzodithiophene (BDT), fluorene, ditheno[3,2-b:2',3'-d]pyrrole, indolo[3,2-b]carbazole, tetraphenylethylene (TPE), and fluoranthene, there is no clear relationship between the structures of the HTMs and the photovoltaic performance of the PSCs [31–36]. There are two common strategies in developing dopant-free HTMs for PSCs. One is to employ planar conjugated core as building block to enhance the hole-carrier mobility. The other strategy applied to improve the hole mobility for dopant-free HTMs is to incorporate an acceptor moiety into the  $\pi$ -bridges to construct a donor–acceptor (D-A) system on the basis of strong dipole–dipole interactions [37]. Although a variety of D-A-structured small molecular materials were specially designed and synthesized [37–39], to the best of our knowledge, none of these D-A-structured materials outperformed the doped spiro-OMeTAD.

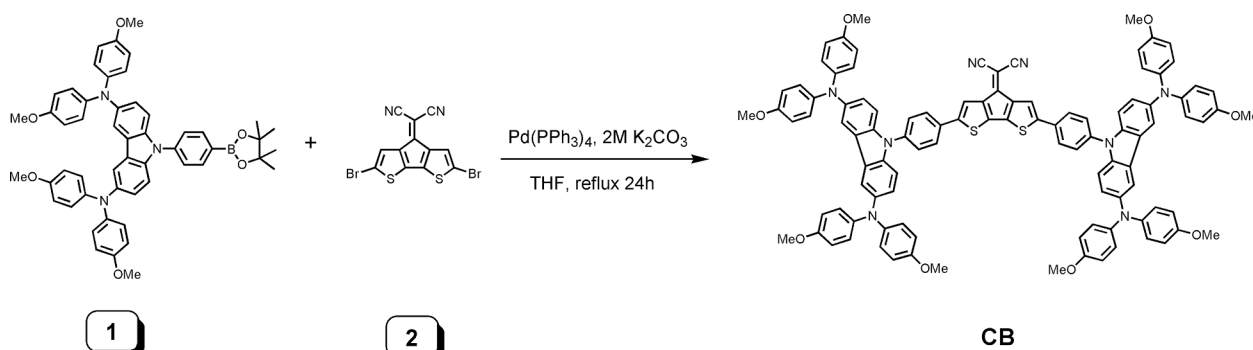
Besides HTM, the fabrication methods of device play a crucial role for the successful commercialization of PSCs. However, the devices with the promising performances are usually prepared by spin-coating process in a glovebox, which may hinder their commercialization due to the waste of materials during device fabrication and uneven surface coverage upon device up-scaling. Printing technique is the most promising alternative for replacing the traditional spin-coating technique in up-scaling. Currently, different deposition techniques, such as slot die [40–42], inkjet printing [43–44], blade-coating [45–50], and roll-to-roll printing [51–52], were developed and drew considerable research attention. Among these techniques, blade-coating method is a simple,

low-cost and effective material-usage technique owing to the rheological properties of the precursor solution. Although the blade-coating technique have been employed for fabricating PSCs, the majority of the reports mainly focus on hole-conductor-free, carbon-based mesoscopic scaffolds or planar *p-i-n* inverted organic solar cell configuration [53–55]. In contrast, there have been few studies with printable *n-i-p* PSCs architectures owing to the lack of suitable HTMs [56].

The cyclopenta[2,1-b:3,4-b']dithiophene (CPDT) unit is a thiophene-based  $\pi$ -conjugated systems with rigid structure, implying a greater planarity and longer  $\pi$ -conjugation of the bridging units which may facilitate intermolecular  $\pi$ – $\pi$  packing interactions and S...S interactions in the solid state, leading to efficient charge transport [57]. As a result, CPDT derivatives have been widely applied in various photovoltaic applications, including dye-sensitized solar cells (DSSCs), organic field-effect transistors (OFETs), and organic photovoltaics (OPVs) [58–60]. In this regard, CPDT-based HTMs could be excellent candidates for PSCs. Several CPDT derivatives have been used as HTM to give efficient PSCs. For example, Nazeeruddin et al reported in 2016 a molecularly engineered spiro-shaped molecule based on fluorene–dithiophene (FDT) core carrying two triphenylamine (TPA) arms via a fluorene bridge as the HTM, affording an impressive PCE of 20.2% [61]. Very recently, we synthesized various two-dimensional CPDT derivatives and applied them as HTM in PSCs fabrication, yielding PCEs of 14.41–18.03% [62–65]. Nevertheless, all of these CPDT-based HTMs gave a high performance only in combination with several dopants.

We previously reported the use of thermal-assisted blade-coating (TABC) method to prepare high quality perovskite film together with doped spiro-OMeTAD as HTM layer in *n-i-p* PSCs, a high PCE of 17.55% was achieved [66–67]. However, the above doped HTM was fabricated via conventional spin-coating process in a glove box, which is adverse to fabricate large-area PSCs. Furthermore, the presence of the additives in HTM notoriously increases the hydrophilicity and thus decreases the stability of the resulted PSCs [12–16]. So far, very few alternative small-molecules can replace the benchmark spiro-OMeTAD in a fully printed *n-i-p* PSCs. Qin et al. in 2017 reported a fully printed PSCs fabricated by slot-die-coated 2,2',7,7'-tetrakis(*N,N*-di-*p*-methoxyphenyl) amine-9,9'-bifluorenylidene (Bifluo-OMeTAD) film as the HTM with a performance of 14.75%, which is higher than that of the state-of-the-art spiro-OMeTAD reference cell (11.70%) under the similar condition. However, Bifluo-OMeTAD requires chemical dopants in order to enhance the hole conductivity for the achieved performance [56]. Thus, there is a strong need in developing compatible dopant-free HTM for high-efficiency printed PSCs.

In this work, we demonstrate the fabrication of PSCs devices based on a donor–acceptor-donor (D-A-D) HTM **CB** without using dopants. The perovskite films were formed by TABC process. The **CB** is a new class of small-molecule-based HTM with the 4-dicyanomethylene-cyclopenta[2,1-b:3,4-b']dithiophene (diCN-CPDT) moiety as the acceptor unit in



Scheme 1. Synthetic route for CB.

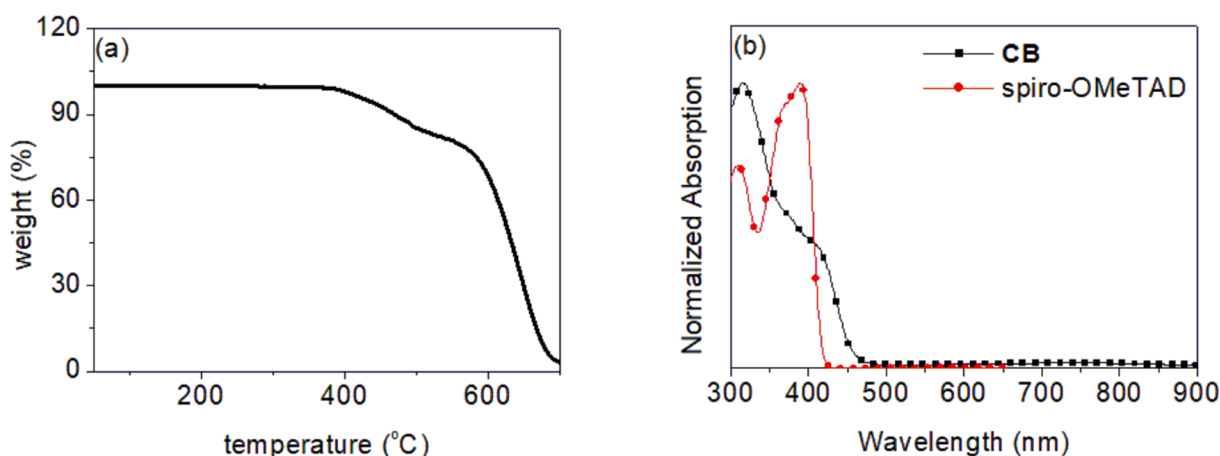


Fig. 2. (a) TGA curve and (b) Normalized absorption spectra of CB and spiro-OMeTAD in chlorobenzene solution.

Table 1

Photophysical and electrochemical data of CB and spiro-OMeTAD.

HTM	$\lambda_{\text{abs}}^{\text{a}}$ (nm) ( $\epsilon \times 10^{-4}/\text{M}^{-1} \text{cm}^{-1}$ )	$\lambda_{\text{f}}^{\text{a}}$ (nm)	$E_{\text{HOMO}}^{\text{b}}$ (eV)	$E_{0-0}^{\text{c}}$ (eV)	$E_{\text{LUMO}}^{\text{d}}$ (eV)	$I_{\text{p}}^{\text{e}}$ (eV)	$E_{\text{HOMO}}^{\text{f}}$ (eV)	$E_{\text{LUMO}}^{\text{f}}$ (eV)
CB	315 nm (11.1)	462	-5.30	2.88	-2.42	-5.11	-4.33	-1.77
spiro-OMeTAD	389 nm (18.37)	428	-5.15	3.02	-2.13	-5.10	-4.21	-0.61

<sup>a</sup> The absorption and fluorescence maximum measured in chlorobenzene solution.<sup>b</sup> Determined from the differential pulse voltammetry.<sup>c</sup> The value of  $E_{0-0}$  obtained from the intersection of normalized absorption and fluorescence spectra.<sup>d</sup> Energy of the LUMO of the compounds estimated by  $E_{\text{HOMO}} + E_{0-0}$ .<sup>e</sup> Ionization potential measured by the photoemission in air method from films.<sup>f</sup> Values calculated at DFT/B3LYP/6-31G(d,p) level.

the central building block with two bis(*p*-methoxyphenylamino)-substituted carbazole as the donor groups, as shown in Fig. 1. The cyclopenta[2,1-*b*:3,4-*b'*]dithiophene is selected as the central core owing to its high co-planarity, which enhances  $\pi$ - $\pi$  stacking interactions, thereby facilitating charge transport. The devices fabricated with TABC process of dopant-free CB for fully printed PSCs except for electrodes using a structure of FTO glass/c-TiO<sub>2</sub>/mp-TiO<sub>2</sub>/CH<sub>3</sub>NH<sub>3</sub>PbI<sub>3</sub>/CB/Ag exhibited excellent PCE of 21.09%, which is higher than doped spiro-OMeTAD-based device (14.28%) under the same fabricating condition. This is the highest PCE ever reported for a fully printable *n-i-p* type PSCs with dopant-free HTM. Most importantly, it was found the fully printed PSCs based on dopant-free CB HTM exhibited better long-term stability than the device based on spiro-OMeTAD under ambient conditions with a relative humidity (RH) of ~50%. In addition, the dopant-free CB-based device can retain 94% of its initial PCEs after 500 h of storage. Therefore, CB has a great potential to be used as non-doped HTM for high-performance, fully printable PSCs

with outstanding long-term stability.

## 2. Results and discussion

The synthetic route of CB is illustrated in Scheme 1, and the experimental details are provided in the Supporting Information. The hole-transporting material CB was prepared from carbazole-based pinacolboronates (1) [62] by Pd(0)-mediated Suzuki coupling reaction with 2-[2,6-Dibromo-4H-cyclopenta[2,1-*b*:3,4-*b'*]dithiophene-4-ylidene] malononitrile (2) [68]. This compound was purified by column chromatography and characterized by <sup>1</sup>H/<sup>13</sup>C NMR spectroscopy and mass spectrometry (see the Supporting Information). The thermogravimetric analysis (TGA) is shown in Fig. 2a. CB exhibits excellent thermal stability, with 5% weight-loss temperatures (*T*<sub>d</sub>) exceeding 431 °C, which is higher than that of spiro-OMeTAD (417 °C) [69], suggesting good thermal stability. However, a glass transition endotherm was not detected for CB in the explored temperature range.

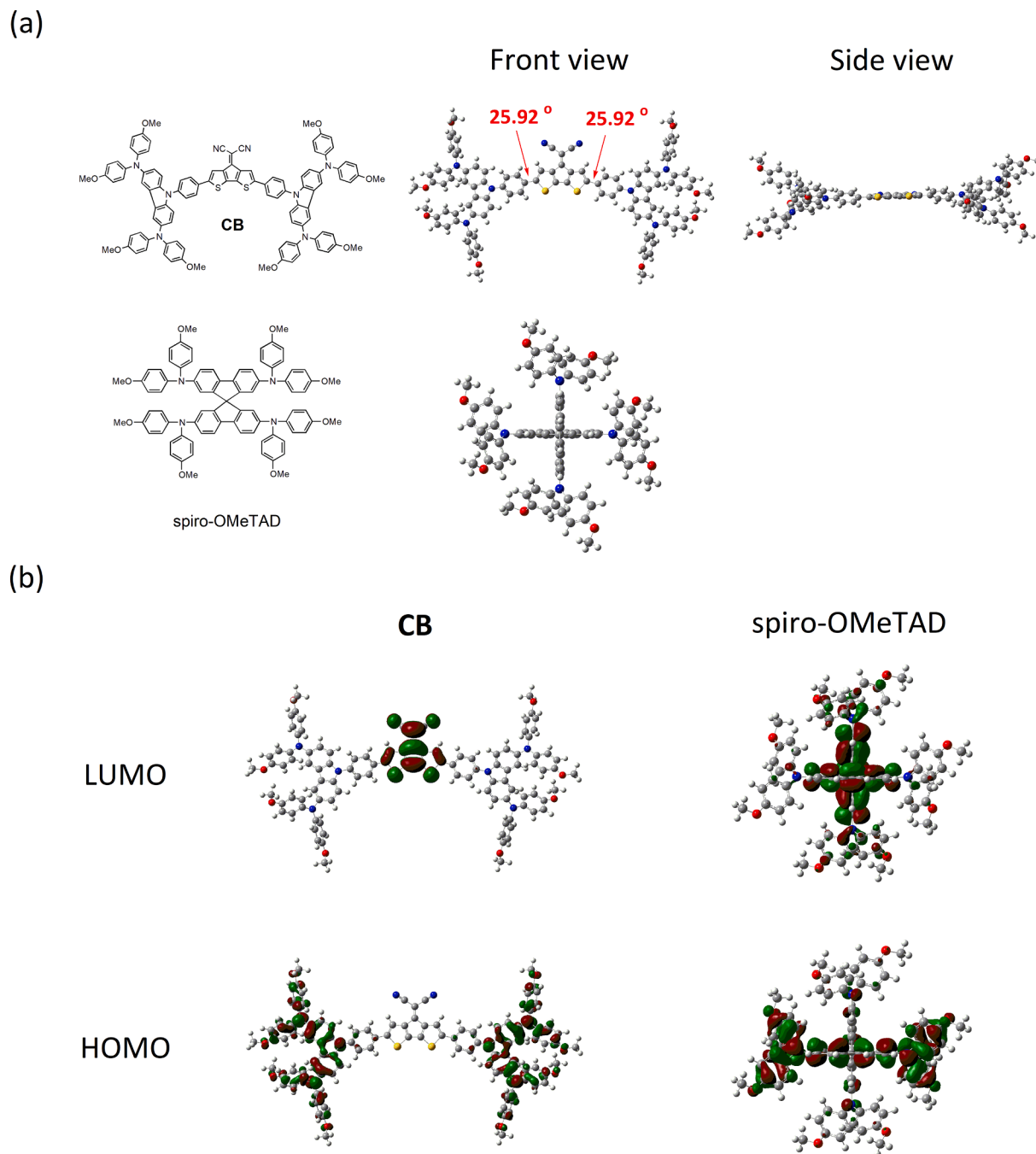


**Fig. 3.** (a) Optimized structures of **CB** and spiro-OMeTAD calculated with DFT on B3LYP/6-31G(d,p) and (b) The electron densities of HOMO and LUMO level of **CB** and spiro-OMeTAD.

The normalized UV–vis absorption spectra of **CB** and spiro-OMeTAD in chlorobenzene are depicted in Fig. 2b and the photophysical data are summarized in Table 1. Compound **CB** shows an intense absorption in the UV region with absorption maximum at 315 nm, which is assigned to  $\pi$ - $\pi^*$  transition of the  $\pi$ -conjugated system. However, a relatively weak absorption band centered around  $\sim$ 695 nm is ascribed to the intramolecular charge transfer (ICT) band from the carbazole-substituted donor to the central diCN-CPDT acceptor moiety. To further analyze the absorption properties of HTM **CB**, the absorption spectrum and vertical energies of **CB** was calculated with time-dependent density functional theory (TDDFT)-B3LYP functional in combination with the standard 6-31G(d,p) basis set. The simulated absorption spectrum is presented in Fig. S1 in the Supporting Information. The TDDFT excited states calculations were performed on the lowest 10 singlet-singlet

excitations of HTM **CB**, neglecting the influence of solvent. The results of transitions with oscillator strength above 0.1 are summarized in Table S1 in the Supporting Information, except the lowest transition for **CB** in order for comparison. The calculated absorption spectrum of **CB** exhibits strong absorption peak in the visible region, which is associated with  $\pi$ - $\pi^*$  transitions. While the weak absorption band with low oscillator strength ( $f = 0.068$ ) was observed at the longer wavelength, which could arise from the ICT band.

To gain a deeper insight in structure–property correlation, the optimized structure of **CB** and electron density distribution of frontier orbitals of **CB** and spiro-OMeTAD were carried out by density functional theory (DFT) calculation. As presented in Fig. 3a, **CB** shows a small dihedral angle of  $25.92^\circ$  between the diCN-CPDT core and the attached carbazole arms, indicating a near planar conjugated geometry, which is

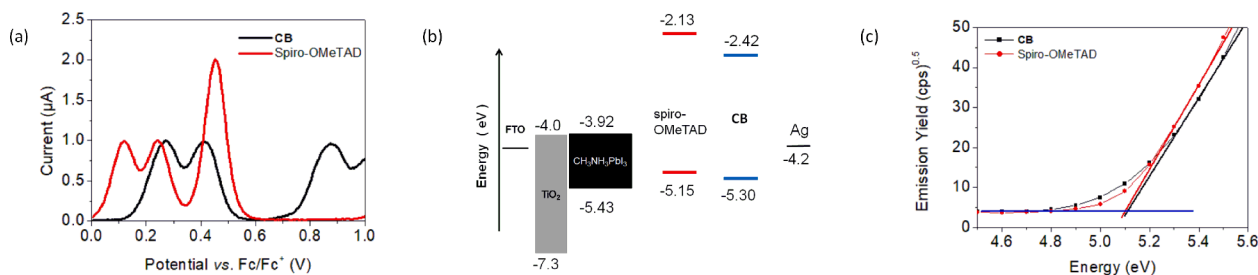


Fig. 4. (a) Normalized differential pulsed voltammetry (DPV) of **CB** and spiro-OMeTAD in THF solution, (b) Energy level diagram of **CB** and spiro-OMeTAD used in perovskite solar cells and (c) Photoemission yield spectra of **CB** and spiro-OMeTAD in air.

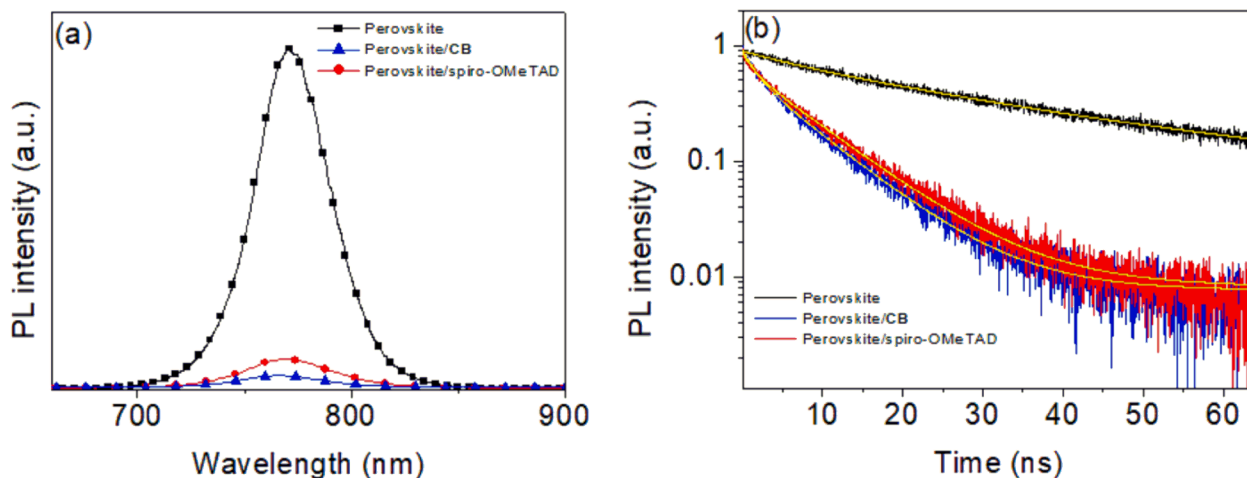


Fig. 5. (a) Steady-state photoluminescence (PL) spectra of the perovskite film, perovskite/**CB** film, and perovskite/spiro-OMeTAD film and (b) Time-resolved photoluminescence (TRPL) spectra of the perovskite film, perovskite/**CB** film, and perovskite/spiro-OMeTAD film.

Table 2

Summary of the fitting results and corresponding dynamic parameters derived from TRPL decay traces.

HTM	A <sub>1</sub>	τ <sub>1</sub> (ns)	A <sub>2</sub>	τ <sub>2</sub> (ns)	τ <sub>avg.</sub> (ns)
none	0.254	8.21	0.746	35.78	28.78
<b>CB</b>	0.421	1.58	0.579	7.88	5.23
spiro-OMeTAD	0.366	1.725	0.634	10.583	7.34

Table 3

Photovoltaic parameters of PSCs based on dopant-free **CB** and doped spiro-OMeTAD as HTMs fabricated by spin-coating and TABC methods.

HTM	Preparation method	V <sub>oc</sub> [V]	J <sub>sc</sub> [mA cm <sup>-2</sup> ]	FF (%)	PCE <sub>max</sub> [%]
<b>CB</b>	A <sup>a</sup>	1.15	23.72	76.1	20.76
<b>CB</b>	B <sup>b</sup>	1.15	23.60	77.7	21.09
spiro-OMeTAD	A <sup>a</sup>	1.13	23.71	74.8	20.04
spiro-OMeTAD	B <sup>b</sup>	1.03	19.51	71.1	14.28

<sup>a</sup> Method A: **CB** and spiro-OMeTAD were deposited by spin-coating method.

<sup>b</sup> Method B: **CB** and spiro-OMeTAD were deposited by TABC method.

beneficial to intermolecular stacking, and thus hole transport process. Whereas the spiro-OMeTAD has two fluorene units orthogonal to each other. In addition, the HOMO is distributed mainly on the donor end-groups, while the LUMO is localized on the central core acceptor, so that the charges are clearly transferring from the donor to the acceptor with the aid of the bridge (Fig. 3b). Furthermore, the calculated HOMO and LUMO energy levels of **CB** and spiro-OMeTAD were determined to

be  $-4.33/-1.77$  and  $-4.21/-0.61$  eV, respectively. Consequently, the energy gaps of **CB** and spiro-OMeTAD were calculated to be 2.56 and 3.60 eV, respectively.

To evaluate the energy levels alignment of **CB** with perovskite, the differential pulse voltammetry (DPV) was performed in THF solution ( $1.0 \times 10^{-3}$  M) and the results are shown in Fig. 4a, and the redox parameters are collected in Table 1. The energy level diagram of **CB** and spiro-OMeTAD are plotted in Fig. 4b. The HOMO energy level of **CB** was determined to be  $-5.30$  eV, which is deeper than that of spiro-OMeTAD ( $-5.15$  eV). The HOMO value is more positive than that of perovskite material ( $-5.43$  eV), suggesting effective hole-extraction capability from the perovskite to **CB**. Moreover, the LUMO level of  $-2.42$  eV for **CB**, as calculated from its optical band gap and HOMO level, is sufficiently higher than that of perovskite ( $-3.93$  eV). As a result, it will effectively block the undesired electron transfer from perovskite to Ag counter electrode, and thus reduce charge recombination in the device. For comparison, we measured solid-state ionization potential ( $I_p$ ) values of **CB** and spiro-OMeTAD in film states using photoelectron spectroscopy in air (PESA) and the results are presented in Fig. 4c. The measured  $I_p$  value of **CB** was found to be  $-5.11$  eV, which was close to that of spiro-OMeTAD ( $-5.10$  eV).

In order to explore the hole-transport ability of different HTMs, the hole mobilities of **CB** and spiro-OMeTAD were measured using the space-charge-limited current (SCLC) method in the  $J$ - $V$  characteristics under dark condition, as shown in Fig. S2 in the Supporting Information. Without adding any dopant, the value of hole mobility obtained for pristine **CB** is  $2.97 \times 10^{-4}$  cm<sup>2</sup> V<sup>-1</sup> s<sup>-1</sup>, which is higher than that of doped spiro-OMeTAD ( $2.38 \times 10^{-4}$  cm<sup>2</sup> V<sup>-1</sup> s<sup>-1</sup>). This result reveals the potential of compound **CB** to be used as dopant-free HTM in PSCs. The improved charge hopping property may be attributed to the donor-acceptor type structure of **CB** molecule.

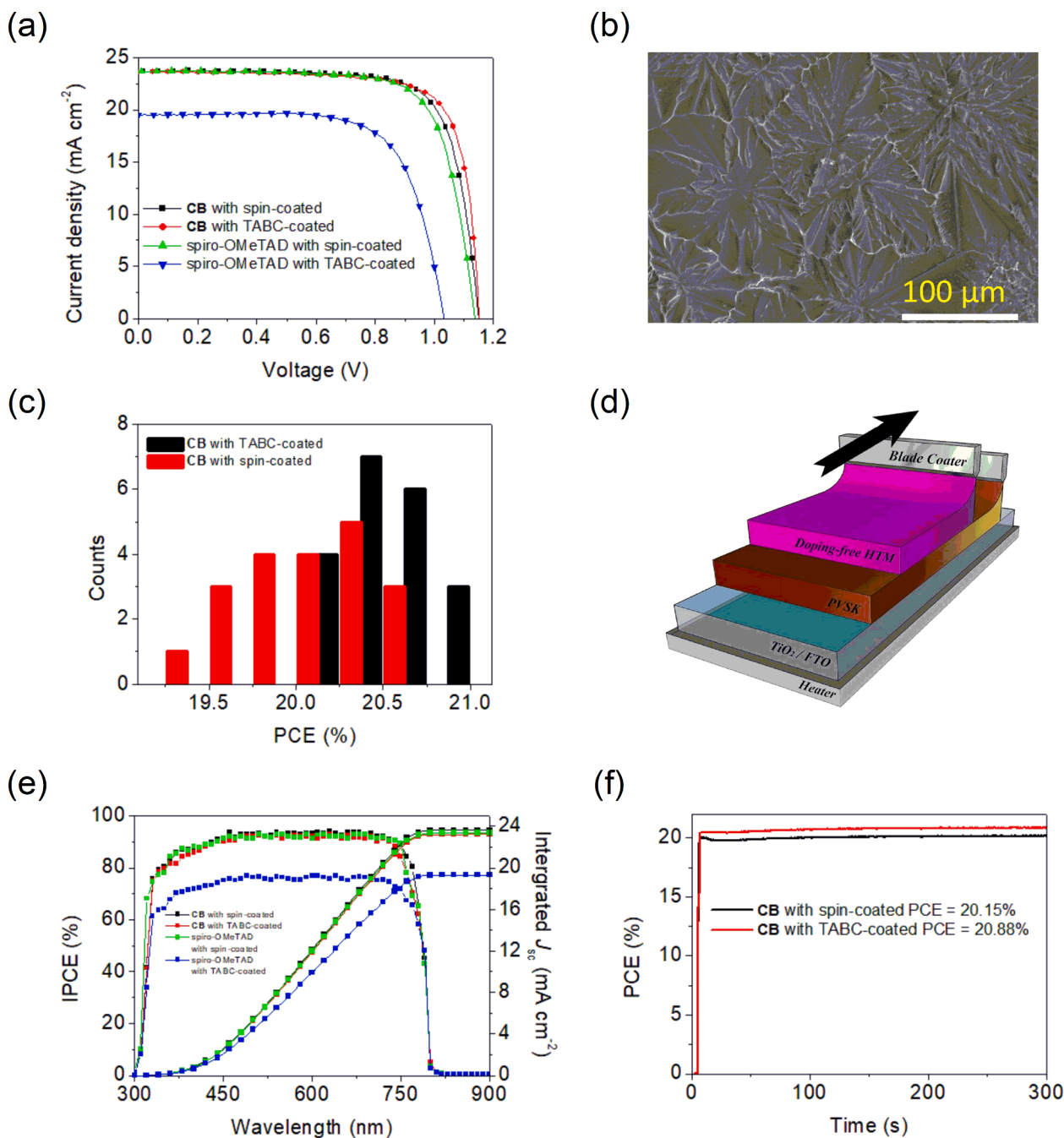


**Fig. 6.** (a)  $J$ - $V$  curves of devices at reverse scan based on dopant-free CB and doped spiro-OMeTAD as HTMs fabricated by spin-coating and TABC methods, (b) The top-view SEM image of the perovskite film prepared by TABC method, (c) Histogram of PCEs for PSCs fabricated from CB by TABC method and spin-coating, (d) Schematic illustration of the sequential deposition of perovskite and HTMs films via TABC method, (e) Corresponding IPCE spectra and integrated photocurrent for devices with dopant-free CB and doped spiro-OMeTAD layers by spin-coating and TABC methods, (f) Stable power output of CB-device fabricated by spin-coating and TABC methods.

To further explore the hole-extraction ability of CB and spiro-OMeTAD at the interface between the perovskite and different HTMs, the steady-state photoluminescence (PL) and time-resolved photoluminescence (TRPL) measurements were conducted on the samples of glass/ $\text{CH}_3\text{NH}_3\text{PbI}_3$  with and without HTMs. As shown in Fig. 5a, the bare perovskite film exhibited a strong PL signal at 770 nm. When the perovskite layer was covered by various HTMs, the intensities of PL emission were significantly reduced. The perovskite films capped with CB showed more PL quenching ( $\sim 96\%$ ) than the films capped with spiro-OMeTAD ( $\sim 91\%$ ), indicating the superior hole-extraction ability from perovskite film. This may result from the stronger  $\text{Pb}\cdots\text{S}$  interaction

exists between the thiophene-rich skeleton and the perovskite [70]. Time-resolved PL decay were also carried out. As shown in Fig. 5b and Table 2, the pure perovskite film on glass showed a slow average decay time of 28.78 ns. With the CB and spiro-OMeTAD coated on perovskite layer, the decay time considerably decreased to 5.23 and 7.34 ns, respectively. Thus the perovskite/CB bi-layered films showed shorter lifetime in comparison with perovskite/spiro-OMeTAD films, suggesting an outstanding hole-extraction ability of CB and its potential to serve as HTM for PSC fabrication. Furthermore, the hole-transport yield ( $\Phi_{\text{ht}}$ ) with and without HTMs were determined using the following equation [71–72]:

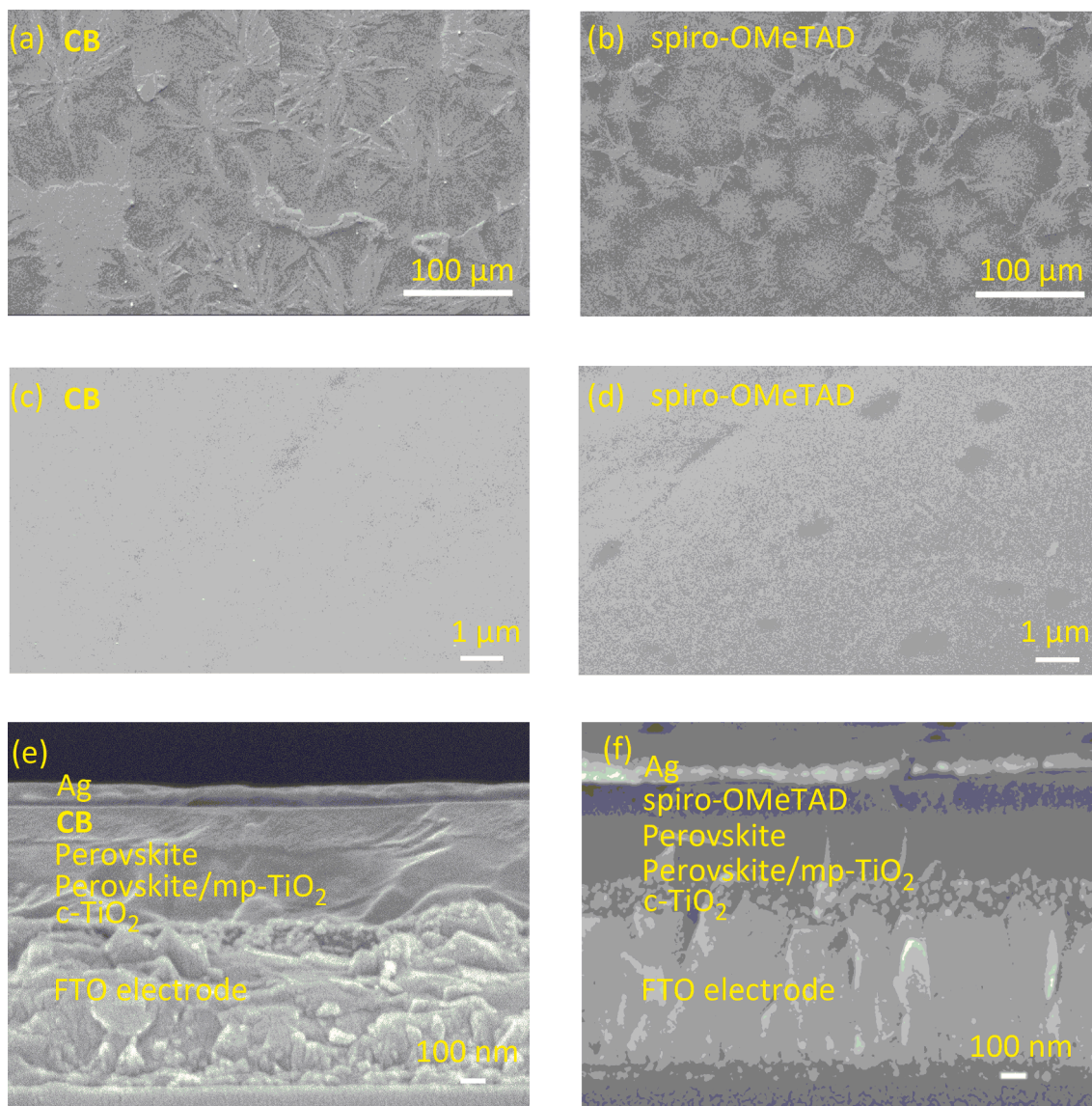


**Fig. 7.** The top-view SEM images of (a) **CB** and (b) spiro-OMeTAD on the underlying perovskite film fabricated by TABC method; A zoomed-in SEM images of (c) **CB** and (d) spiro-OMeTAD on the underlying perovskite film fabricated by TABC method; Cross-sectional SEM images of the fully printed PSCs devices with (e) **CB** and (f) spiro-OMeTAD HTMs.

$$\Phi_{ht} = 1 - \tau_h/\tau_p \quad (1)$$

where  $\tau_h$  is the average lifetime for glass/perovskite/HTM, and  $\tau_p$  is that for glass/perovskite. The hole-transport yields of glass/perovskite/**CB** and glass/perovskite/spiro-OMeTAD, as calculated from eq (1), are 82% and 74%, respectively. In accord with a larger PL intensity quenching, the  $\Phi_{ht}$  value for glass/perovskite/**CB** is larger than that of glass/perovskite/spiro-OMeTAD. This might also account for a more efficient hole transfer from perovskite to **CB**.

To explore the device performance of PSCs based on **CB** as dopant-free HTM, the conventional *n-i-p* device configuration of FTO glass/c-TiO<sub>2</sub>/mp-TiO<sub>2</sub>/CH<sub>3</sub>NH<sub>3</sub>PbI<sub>3</sub>/**CB**/Ag was constructed, with the perovskite layer prepared by TABC method and the **CB** layer by spin-coating. The details of device fabrication are provided in [Supporting Information](#). As a comparison, doped spiro-OMeTAD HTM was employed as a reference to prepare the device under the same conditions. The optimized photovoltaic device data are summarized in [Table 3](#) and the corresponding current-voltage (*J-V*) characteristics measured under 100 mW cm<sup>-2</sup> AM 1.5G illumination for reverse scan condition are shown in [Fig. 6a](#). The cross-section scanning electron microscopy (SEM)

image of a PSCs with spin-coated **CB** HTM is shown in [Fig. S3](#). A clear layer-by-layer structure can be observed. A ~250 nm-thick **CB** layer was uniformly formed on top of the perovskite layer. In addition, the surface morphologies of perovskite films with or without HTMs were also probed by SEM measurement. The bare perovskite film, prepared by TABC method at 130 °C following to our previous processes, gave a dense and large crystal domain size (300–400 μm) without evident pinholes and voids ([Fig. 6b](#)) [66–67], where the grain boundaries of spherulites were seen on the surface. The formation of spherulites were presumably attributed to the rapid volatilization of the solvent at high temperature during the crystallization process of the perovskite film. For the growth mechanism of spherulites, the primary nucleus grows in all directions to form the radial crystallites. The radial crystallites continue to grow outward until they touch adjacent crystals. The sizes and shapes of spherulites depend on an interaction between the crystal nuclei, the crystal growth velocity and solvent evaporation rate. Large-sized spherulites could effectively improve the photovoltaic performance of PSCs [73]. In contrast, the top-view SEM images of spin-coated **CB** and spiro-OMeTAD films on top of the perovskite layer showed a full coverage ([Fig. S4](#)). The device with spin-coated dopant-free **CB** achieved

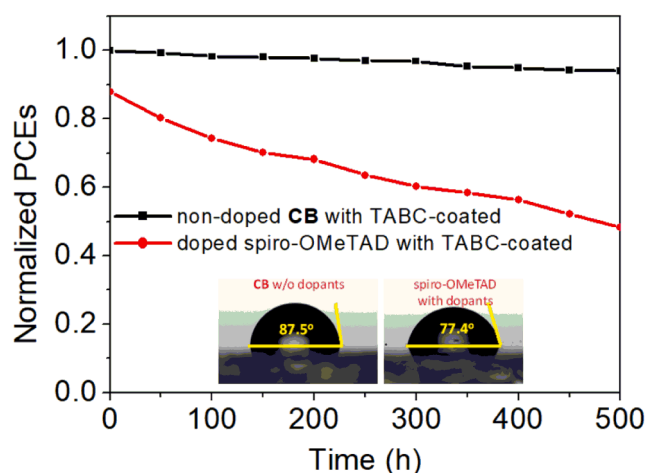


Fig. 8. Normalized PCEs of the devices with pristine CB and doped spiro-OMeTAD layers.

an encouraging PCEs of 20.76%, together with a  $J_{sc}$  of  $23.72 \text{ mA cm}^{-2}$ , a  $V_{oc}$  of 1.15 V and an FF of 0.76, which is comparable to that of the device employing spin-coated doped spiro-OMeTAD (20.04%). A batch of 20 cells were fabricated to analyze the distribution and reproducibility of photovoltaic metrics (Fig. 6c). An average PCE of 19.98% for dopant-free CB-based PSCs was observed, indicating the good reproducibility. These results demonstrate that CB is a promising candidate as dopant-free HTM for high-performance PSCs.

To explore the feasibility of fully printed PSCs, the same device structure (*n-i-p* configuration) with perovskite and HTM layers both prepared by TABC method were constructed (the detail information described in the Supporting Information) [66–67]. The schematic sequential deposition of perovskite and HTMs thin films via TABC method was conducted as depicted in Fig. 6d. To optimize the property of dopant-free CB as HTM by TABC method, the CB films were coated at different substrate temperatures range from 70 to  $130 \text{ }^\circ\text{C}$ . As shown in Fig. S5, the PCE increased on going from 70 to  $110 \text{ }^\circ\text{C}$  and then decreased on going to  $130 \text{ }^\circ\text{C}$ , suggesting some interfacial film structure variation and the interface between the perovskite and CB has the best contact under  $110 \text{ }^\circ\text{C}$  process. The surface morphologies of the TABC-based HTM layers at various substrate temperatures were examined by SEM. It was observed that the film morphology of HTM film on perovskite layers are highly influenced by the substrate temperature. As

shown in Fig. S6, the films prepared at a lower substrate temperature ( $70\text{--}90 \text{ }^\circ\text{C}$ ) showed a small lamellar morphology. At the substrate temperature of  $110 \text{ }^\circ\text{C}$ , large and perfectly lamellar morphology was obtained, indicating the better-contacted HTM on the perovskite layer. However, as the temperature was increased to  $130 \text{ }^\circ\text{C}$ , the island-like morphology with obvious film cracks were observed onto the perovskite films. Therefore, the HTM films were prepared at the optimized substrate temperature of  $110 \text{ }^\circ\text{C}$ . Encouragingly, the best PCE was 21.09% with an open-circuit voltage ( $V_{oc}$ ) of 1.15 V, a short-circuit current density ( $J_{sc}$ ) of  $23.60 \text{ mA cm}^{-2}$ , and a fill factor (FF) of 0.78. (Fig. 6a), which is comparable to the PCE of spin-coated CB-based PSCs (20.76%). In contrast, the same TABC-processed doped spiro-OMeTAD-based device exhibited an inferior efficiency of 14.28%, with a  $V_{oc}$  of 1.03 V, a  $J_{sc}$  of  $19.51 \text{ mA cm}^{-2}$  and an FF of 0.71 (Fig. 6a). The lower PCE of device based on spiro-OMeTAD via TABC method was presumably attributed to some extent evaporation of *t*-BP (the only liquid in device) at higher preparation temperature ( $110 \text{ }^\circ\text{C}$ ), and thus the optimized ratio of *t*-BP/Li-TFSI may be changed [74–76]. The concentration change of additives is more pronounced for the device performance, and it can lead to poor diffusion for excitons at the perovskite/HTMs interfaces and induce recombination so that a loss in the  $V_{oc}$  and FF was observed. These results demonstrated that the CB is a promising material to be used for dopant-free TABC-printed PSCs and holds potential for large-scale PSCs by printing method. To the best of our knowledge, this is the first report on fully printed *n-i-p* PSCs based on dopant-free HTM/perovskite layer giving a remarkable performance. Furthermore, the CB-based PSCs showed a small hysteresis between the forward and reverse scans (Fig. S7), which may be attributed to higher hole mobility and efficient hole-extraction ability (Fig. S2 and Fig. 5). The corresponding incident photo-to-electron conversion efficiency (IPCE) of the fully printed PSCs devices are displayed in Fig. 6e. The integrated current densities for non-doped CB and doped spiro-OMeTAD are  $23.20$  and  $19.44 \text{ mA cm}^{-2}$ , respectively, which are consistent with the  $J_{sc}$  values measured in *J-V* scans. The steady-state power output was also measured for 300 s at the maximum power point (MPP) to confirm the accuracy of the measured PCEs (Fig. 6f). The stabilized PCEs of 20.88% for fully PSCs based on CB without dopants, indicating good device stability. In addition, the histogram of PCEs measured for 20 devices of dopant-free CB via TABC technique are shown in Fig. 6c. The CB-based devices exhibited average PCEs values of 20.60%, indicating good reproducibility for the devices fabricated by TABC method and even better than the reproducibility of devices with spin-coated CB.

To better understand the correlation between device performance

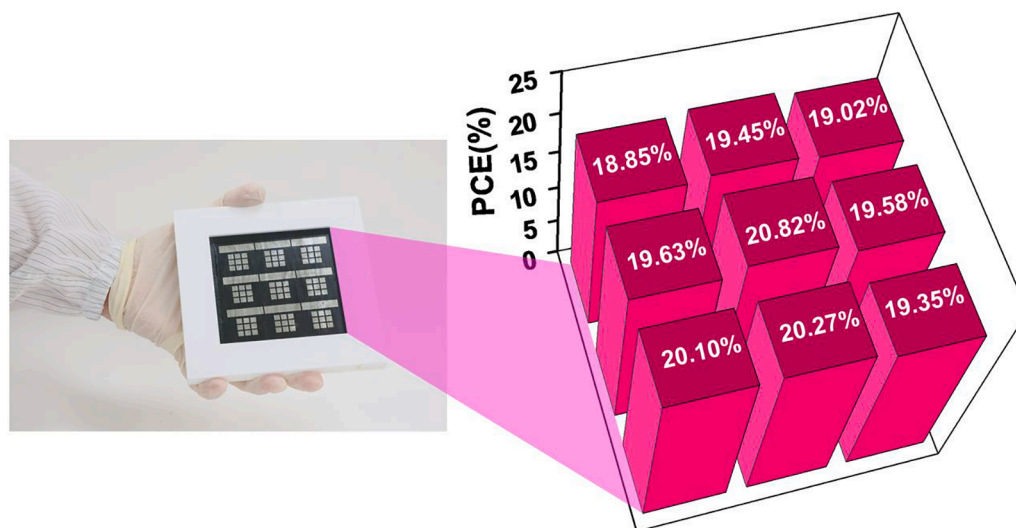


Fig. 9. Schematic illustration of the PCE distribution estimation, and photos of  $10 \text{ cm} \times 10 \text{ cm}$  large-area devices fabricated by TABC method.

and the HTM films formation by TABC process, the surface morphology of HTM films deposited onto the perovskite layers were further examined by SEM (Fig. 7a-d) and atomic force microscope (AFM) in Fig. S8. The top-view SEM image indicates a full coverage of HTM films on the perovskite layer, and the images showed that the HTM layer follows the pattern of the layer underneath with spherulites and lamellar morphology of perovskite (Fig. 6b). The larger amount of lamellar-like morphology are evident for CB coated film compared to spiro-OMeTAD coated film (Fig. 7a and b), which may suggest that there is the better-contacted CB film on the perovskite layer, favoring the charge extraction and transport. As presented in the magnified SEM images in Fig. 7c and d, pinholes could be detected on the surface of the spiro-OMeTAD film, while the perovskite layer was uniformly covered by a thin layer of CB without any observable particles or pinholes, indicating that this helps to reduce the charge recombination losses at the perovskite/CB interface and to improve the photovoltaic performance and stability of the devices. Although the AFM images of the HTM films revealed that the root-mean-square (RMS) roughness of CB film (41.6 nm) is larger than spiro-OMeTAD film (12.4 nm), the high-quality films of CB were observed without aggregates as disclosed in the AFM images in Fig. S8. In addition, the cross-sectional SEM image of CB- and spiro-OMeTAD-based PSCs are shown in Fig. 7e and f. The optimized thickness of dopant-free CB layer is estimated to be ~200 nm, which is thinner than that prepared by spin-coating (Fig. S3). CB-based device exhibited better performance may be attributed to the superior hole mobility (Fig. S2), lower charge recombination (Fig. 5), and the better contact between the perovskite layer and HTM film (Fig. 7a).

The device stability is another vital property to address before commercialization of PSCs. We evaluated the long-term stability of non-doped CB-based PSCs and doped spiro-OMeTAD-based PSCs, all fabricated by TABC method. The durability test was conducted in ambient condition with ~50% relative humidity without encapsulation (Fig. 8). Encouragingly, the device employing pristine CB maintained 94% of the initial PCE after 500 h of aging, whereas the PSCs based on doped spiro-OMeTAD showed significantly lower efficiency, 55% of the initial values, after 500 h. The drop in PCE might be attributed to the hygroscopic nature of Li-TSFI dopant (as discussed later). It is generally suggested that a more hydrophobic character of HTM film should benefit the device stability, because the HTM film can better protect the perovskite layer from the moisture penetration. For this, we measured the water contact angles on the CB and spiro-OMeTAD films. As shown in the inset of Fig. 8, a much higher angle of 87.5° was observed on the dopant-free CB film. In contrast, the water contact angle on doped spiro-OMeTAD is even lower (77.4°). These results corroborate with the stability data obtained from the devices and demonstrate the potential of CB molecule as a superior candidate as HTM.

Furthermore, the large-area (100 cm<sup>2</sup>) perovskite and HTM layer prepared by TABC method were examined for the film uniformity. By using a shadow mask, the film was divided into 9 areas, and from each area, 9 subcells with an effective area of 0.16 cm<sup>2</sup> for each were prepared. The PCEs for all the subcells were measured averaged for each area and the results are shown in Fig. 9. The overall average PCE for all the areas was 19.67%, and the highest PCE (20.82%) was obtained from the area located at the center of the film, while those from the edge areas exhibited slightly low PCE values. Therefore, TABC method enables the formation of a smooth film for equally high-performing subcells to be made across the whole area. It shows that the both perovskite and HTM layer prepared by TABC process improve the uniformity and reproducibility to make them a step closer to large-scale manufacturing.

### 3. Conclusion

In conclusion, we have synthesized a new HTM CB and demonstrated that high-efficiency PSCs were achieved with it. The CB molecule exhibits an HOMO energy level matching with that of perovskite, along with good thermal stability over 430 °C. In addition, pristine CB presents

higher hole mobility of  $2.97 \times 10^{-4} \text{ cm}^2 \text{ V}^{-1} \text{ s}^{-1}$  compared to doped spiro-OMeTAD ( $2.38 \times 10^{-4} \text{ cm}^2 \text{ V}^{-1} \text{ s}^{-1}$ ), indicating that CB is a potential dopant-free HTM for PSCs. Furthermore, the strong hole extraction capability of CB was observed by steady-state photoluminescence and time-resolved photoluminescence spectra. With highly uniform and crystalline perovskite film prepared by TABC process and spin-coated pristine CB layer, we achieved a champion PCEs up to 20.76%. More importantly, the CB layer can be prepared by TABC method, allowing a fully printed PSCs to be made. An excellent PCE of 21.09% with a  $J_{sc}$  of 23.60 mAcm<sup>-2</sup>, a  $V_{oc}$  of 1.15 V, and an FF of 0.78 was achieved without using dopant in CB layer. To the best of our knowledge this is the first report with such a high PCE obtained from a fully printed PSCs without using dopant in the HTM layer. We also demonstrated that the device with pristine CB layer exhibited a remarkably improved stability than the device with doped spiro-OMeTAD, retaining over 90% of its initial performance after 500 h. These results demonstrated that CB is a promising HTM for fabrication of highly efficient and stable PSCs, with the potential to be used in large-scale perovskite devices by printing process.

### 4. Experimental section

**Materials:** The Suzuki coupling reaction was carried out under a nitrogen atmosphere. The products were purified by column chromatography using silica gel. <sup>1</sup>H NMR and <sup>13</sup>C NMR spectra of the new compound CB were recorded with a Bruker 400 MHz spectrometer in dichloromethane-*d*<sub>2</sub> with tetramethylsilane as the internal standard. MALDI-TOF mass spectrometry was carried out with Applied Bio Systems 4800 proteomics analyser. UV spectra were measured in chlorobenzene on a V-550JASCO UV/VIS. Fluorescence spectra were obtained in chlorobenzene on a HITACHI F-4500 fluorescence spectrophotometer. Oxidation and reduction potentials were measured by cyclic voltammetry with a scan rate of 100 mV/s on  $1.0 \times 10^{-3}$  M samples with 0.1 M supporting electrolyte of tetrabutylammonium hexafluorophosphate in THF solution. The reference, working, and auxiliary electrodes were Ag/AgNO<sub>3</sub>, a platinum disk, and a platinum wire, respectively. Photoelectron spectroscopy in air (PESA) was measured by photoelectron spectrometer (AC-2, Riken Reiki).

**Synthesis of CB:** A mixture of **1** (4.35 g, 5.30 mmol), **2** (1 g, 2.51 mmol), Pd(PPh<sub>3</sub>)<sub>4</sub> (0.012 g, 0.10 mmol), 12 mL of 2 M K<sub>2</sub>CO<sub>3</sub> (aq), and 18 mL of THF was refluxed for 16 h under argon. The precipitates were filtered off and the filtrate was concentrated under reduced pressure. The residue was then dissolved in CH<sub>2</sub>Cl<sub>2</sub> and washed with brine. The organic layer was dried over anhydrous MgSO<sub>4</sub> and filtered. The filtrate was concentrated under reduced pressure. Column chromatography with CH<sub>2</sub>Cl<sub>2</sub>/hexane (2:1) as eluent afforded the dark green solid of CB in a yield of 84%. M.P. greater than 300 °C; <sup>1</sup>H NMR (CD<sub>2</sub>Cl<sub>2</sub>, 400 MHz) δ 7.7–7.79 (m, 4H), 7.75–7.77 (m, 2H), 7.58–7.56 (m, 8H), 7.29–7.26 (m, 4H), 7.11–7.08 (m, 4H), 6.95–6.93 (m, 16H), 6.76–6.74 (m, 16H). <sup>13</sup>C NMR (CD<sub>2</sub>Cl<sub>2</sub>, 100 MHz) δ: 155.3, 154.8, 147.3, 145.0, 142.8, 142.5, 142.0, 138.3, 137.6, 132.1, 127.4, 127.0, 125.3, 124.9, 124.6, 119.4, 116.5, 114.9, 113.1, 110.9, 77.6, 55.8. HRMS [MALDI-TOF] *m/z* {M + 1}<sup>+</sup> calcd for C<sub>105</sub>H<sub>78</sub>N<sub>8</sub>O<sub>8</sub>S<sub>2</sub> 1630.5462; found 1630.5445.

### Declaration of Competing Interest

The authors declare that they have no known competing financial interests or personal relationships that could have appeared to influence the work reported in this paper.

### Acknowledgements

Y.-D. Lin thanks the support from Ministry of Science and Technology, Taiwan (Grant Number MOST 109-2113-M-031-007-). K.-M. Lee thanks the support from Ministry of Science and Technology, Taiwan (Grant Number MOST 108-2628-E-182-003-MY3), Chang Gung

University (QZRPD181) and Chang Gung Memorial Hospital, Linkou, Taiwan (CMRPD2J0041).

## Appendix A. Supplementary material

Supplementary data to this article can be found online at <https://doi.org/10.1016/j.cej.2021.131609>.

## References

- [1] A. Kojima, K. Teshima, Y. Shirai, T. Miyasaka, Organometal halide perovskites as visible-light sensitizers for photovoltaic cells, *J. Am. Chem. Soc.* 131 (2009) 6050–6051.
- [2] T. Matsui, T. Yamamoto, T. Nishihara, R. Morisawa, T. Yokoyama, T. Sekiguchi, T. Negami, Compositional engineering for thermally stable, highly efficient perovskite solar cells exceeding 20% power conversion efficiency with 85 °C/85% 1000 h stability, *Adv. Mater.* 31 (2019) 1806823.
- [3] Y. Rong, Y. Hu, A. Mei, H. Tan, M.I. Saidaminov, S.I. Seok, M.D. McGehee, M.E. H. Sargent, H. Han, Challenges for commercializing perovskite solar cells, *Science* 361 (2018) 1–7.
- [4] S. Heo, G. Seo, Y. Lee, M. Seol, S.H. Kim, D.-J. Yun, Y. Kim, K. Kim, J. Lee, J. Lee, W.S. Jeon, J.K. Shin, J. Park, D. Lee, M.K. Nazeeruddin, Origins of high performance and degradation in the mixed perovskite solar cells, *Adv. Mater.* 131 (2019) 1805438.
- [5] NREL, Best Research-Cell Efficiency Chart, <https://www.nrel.gov/pv/cell-efficiency.html> (accessed: May 2021).
- [6] M. Kim, G.-H. Kim, T.K. Lee, I.W. Choi, H.W. Choi, Y. Jo, Y.J. Yoon, J.W. Kim, J. Lee, D. Huh, H. Lee, S.K. Kwak, J.Y. Kim, D.S. Kim, Methylammonium chloride induces intermediate phase stabilization for efficient perovskite solar cells, *Joule* 3 (2019) 2179–2192.
- [7] H. Min, M. Kim, S.U. Lee, H. Kim, G. Kim, K. Choi, J.H. Lee, S.I. Seok, Efficient, stable solar cells by using inherent bandgap of  $\alpha$ -phase formamidinium lead iodide, *Science* 366 (2019) 749–753.
- [8] R. Grisorio, R. Iacobellis, A. Listorti, L. De Marco, M.P. Cipolla, M. Manca, A. Rizzo, A. Abate, G. Gigli, G.P. Suranna, Rational design of molecular hole-transporting materials for perovskite solar cells: direct versus inverted device configurations, *ACS Appl. Mater. Interfaces* 9 (2017) 24778–24787.
- [9] Q. Yan, Y. Guo, A. Ichimura, H. Tsuji, E. Nakamura, Three-dimensionally homojunctioned carbon-bridged oligophenylenevinylene for perovskite solar cells, *J. Am. Chem. Soc.* 138 (2016) 10897–10904.
- [10] Z. Hawash, L.K. Ono, Y. Qi, Moisture and oxygen enhance conductivity of LiTFSI-doped spiro-OMeTAD hole transport layer in perovskite solar cells, *Adv. Mater. Interfaces* 3 (2016) 1600117.
- [11] J. Burschka, F. Kessler, M.K. Nazeeruddin, M. Grätzel, Co(III) complexes as p-dopants in solid-state dye-sensitized solar cells, *Chem. Mater.* 25 (2013) 2986–2990.
- [12] N.J. Jeon, H. Na, E.H. Jung, T.-Y. Yang, Y.G. Lee, G. Kim, H.-W. Shin, S.I. Seok, J. Lee, J. Seo, Fluorene-terminated hole-transporting material for highly efficient and stable perovskite solar cells, *Nat. Energy* 3 (2018) 682–689.
- [13] J.-Y. Seo, H.-S. Kim, S. Akin, M. Stojanovic, E. Simon, M. Fleischer, A. Hagfeldt, S. M. Zakeeruddin, M. Grätzel, Novel p-dopant toward highly efficient and stable perovskite solar cells, *Energy Environ. Sci.* 11 (2018) 2985–2992.
- [14] T. Malinauskas, T.D. Tomkute-Luksiene, R. Sens, M. Daskeviciene, R. Send, H. Wonneberger, V. Jankauskas, I. Bruder, V. Getautis, Enhancing thermal stability and lifetime of solid-state dye-sensitized solar cells via molecular engineering of the hole-transporting material spiro-OMeTAD, *ACS Appl. Mater. Interfaces* 7 (2015) 11107–11116.
- [15] I. Lee, J.H. Yun, H.J. Son, T.-S. Kim, Accelerated degradation due to weakened adhesion from Li-TFSI additives in perovskite solar cells, *ACS Appl. Mater. Interfaces* 9 (2017) 7029–7035.
- [16] Z. Li, C. Xiao, Y. Yang, S.P. Harvey, D.H. Kim, J.A. Christians, M. Yang, P. Schulz, S. U. Nanayakkara, C.-S. Jiang, J.M. Luther, J.J. Berry, M.C. Beard, M.M. Al-Jassim, K. Zhu, Extrinsic ion migration in perovskite solar cells, *Energy Environ. Sci.* 10 (2017) 1234–1242.
- [17] Y.T. Shi, X.Y. Wang, H. Zhang, H.B. Li, H.L. Lu, T.L. Ma, T.C. Hao, Effects of 4-tert-butylpyridine on perovskite formation and performance of solution-processed perovskite solar cells, *J. Mater. Chem. A* 3 (2015) 22191–22198.
- [18] C.G. Wu, C.H. Chiang, Z.L. Tseng, M.K. Nazeeruddin, A. Hagfeldt, M. Grätzel, High efficiency stable inverted perovskite solar cells without current hysteresis, *Energy Environ. Sci.* 8 (2015) 2725–2733.
- [19] G. Li, T.Y. Zhang, Y.X. Zhao, Hydrochloric acid accelerated formation of planar  $\text{CH}_3\text{NH}_3\text{PbI}_3$  perovskite with high humidity tolerance, *J. Mater. Chem. A* 3 (2015) 19674–19678.
- [20] H. Zhang, J. Mao, H. He, D. Zhang, H.L. Zhu, F. Xie, K.S. Wong, M. Grätzel, W.C. H. Choy, A smooth  $\text{CH}_3\text{NH}_3\text{PbI}_3$  film via a new approach for forming the  $\text{PbI}_2$  nanostructure together with strategically high  $\text{CH}_3\text{NH}_3\text{I}$  concentration for high efficient planar-heterojunction solar cells, *Adv. Energy Mater.* 5 (2015) 1501354.
- [21] Y. Cao, Y. Li, T. Morrissey, B. Lam, B.O. Patrick, D.J. Dvorak, Z. Xia, T.L. Kelly, C. P. Berlinguette, Dopant-free molecular hole transport material that mediates a 20% power conversion efficiency in a perovskite solar cell, *Energy Environ. Sci.* 12 (2019) 3502–3507.
- [22] Y. Chen, X. Xu, N. Cai, S. Qian, R. Luo, Y. Huo, S. Tsang, Rational design of dopant-free coplanar D- $\pi$ -D hole transporting materials for high-performance perovskite solar cells with fill factor exceeding 80%, *Adv. Energy Mater.* 9 (2019) 1901268.
- [23] X. Yang, J. Xi, Y. Sun, Y. Zhang, G. Zhou, W.Y. Wong, A dopant-free twisted organic small-molecule hole transport material for inverted planar perovskite solar cells with enhanced efficiency and operational stability, *Nano Energy* 54 (2019) 103946.
- [24] H. Lu, B. He, Y. Ji, Y. Shan, C. Zhong, J. Xu, J. LiuYang, F. Wu, L. Zhu, Dopant-free hole transport materials processed with green solvent for efficient perovskite solar cells, *Chem. Eng. J.* 385 (2020) 123976.
- [25] Z. Li, Y. Tong, J. Ren, Q. Sun, Y. Tian, Y. Cui, H. Wang, Y. Hao, C.-S. Lee, Fluorinated triphenylamine-based dopant-free hole-transporting material for high-performance inverted perovskite solar cells, *Chem. Eng. J.* 402 (2020) 125923.
- [26] L. Duan, Y. Chen, J. Jia, X. Zong, Z. Sun, Q. Wu, S. Xue, Dopant-free hole-transport materials based on 2,4,6-triarylpyridine for inverted planar perovskite solar cells, *ACS Appl. Energy Mater.* 3 (2020) 1672–1683.
- [27] H.D. Pham, T.C.-J. Yang, S.M. Jain, G.J. Wilson, P. Sonar, Development of dopant-free organic hole transporting materials for perovskite solar cells, *Adv. Energy Mater.* 10 (2020) 1903326.
- [28] H. Zhang, M. Liu, W. Yang, L. Judin, T.I. Hukka, A. Priimagi, Z. Deng, P. Vivo, Thionation enhances the performance of polymeric dopant-free hole-transporting materials for perovskite solar cells, *Adv. Mater. Interfaces* (2019) 1901036.
- [29] X. Jiang, X. Liu, J. Zhang, S. Ahmad, D. Tu, W. Qin, T. Jiu, S. Pang, X. Guo, C. Li, Simultaneous hole transport and defect passivation enabled by a dopant-free single polymer for efficient and stable perovskite solar cells, *J. Mater. Chem. A* 8 (2020) 21036–21043.
- [30] J. Wu, C. Liu, B. Li, F. Gu, L. Zhang, M. Hu, X. Deng, Y. Qiao, W. Tan, Y. Tian, B. Xu, Side-chain polymers as dopant-free hole-transporting materials for perovskite solar cells-the impact of substituents' positions in carbazole on device performance, *ACS Appl. Mater. Interfaces* 11 (2019) 26928–26937.
- [31] Y. Chen, X. Xu, N. Cai, S. Qian, R. Luo, Y. Hao, S.-W. Tsang, Rational design of dopant-free coplanar D- $\pi$ -D hole-transporting materials for high-performance perovskite solar cells with Fill factor Exceeding 80%, *Adv. Energy Mater.* (2019) 1901268.
- [32] X. Yin, J. Zhou, Z. Song, Z. Dong, Q. Bao, N. Shrestha, S.S. Bista, R.J. Ellingson, Y. Yan, W. Tang, Dithieno[3,2-b:3',2'-d]pyrrol-core hole transport material enabling over 21% efficiency dopant-free perovskite solar cells, *Adv. Funct. Mater.* 1904300 (2019).
- [33] B. Cai, X. Yang, X. Jiang, Z. Yu, A. Hagfeldt, L. Sun, Boosting the power conversion efficiency of perovskite solar cells to 17.7% with an indolo[3,2-b] carbazole dopant-free hole transporting material by improving its spatial configuration, *J. Mater. Chem. A* 7 (2019) 14835–14841.
- [34] K. Jiang, J. Wang, F. Wu, Q. Xue, Q. Yao, J. Zhang, Y. Chen, G. Zhang, Z. Zhu, H. Yan, L. Zhu, H.-L. Yip, Dopant-free organic hole-transporting material for efficient and stable inverted all-inorganic and hybrid perovskite solar cells, *Adv. Mater.* 1908011 (2020).
- [35] H.D. Pham, L. Gil-Escrig, K. Feron, S. Manzhos, S. Albrecht, H.J. Bolink, P. Sonar, Boosting inverted perovskite solar cell performance by using 9,9-bis(4-diphenylamino)fluorene functionalized with triphenylamine as a dopant-free hole transporting material, *J. Mater. Chem. A* 7 (2019) 12507–12517.
- [36] X. Sun, F. Wu, C. Zhong, L. Zhu, Z. Li, A structure-property study of fluoranthene-core hole-transporting materials enables 19.3% efficiency in dopant-free perovskite solar cells, *Chem. Sci.* 10 (2019) 6899–6907.
- [37] Z. Li, Z. Zhu, C.-C. Chueh, S.B. Jo, J. Luo, S.-H. Jang, A.K.-Y. Jen, Rational design of dipolar chromophore as an efficient dopant-free hole-transporting material for perovskite solar cells, *J. Am. Chem. Soc.* 138 (2016) 11833–11839.
- [38] S. Paek, P. Qin, Y. Lee, K.T. Cho, P. Gao, G. Grancini, E. Oveisi, P. Gratia, K. Rakstys, S.A. Al-Muhtaseb, C. Ludwig, J. Ko, M.K. Nazeeruddin, Dopant-Free hole-transporting materials for stable and efficient perovskite solar cells, *Adv. Mater.* 19 (2017) 1606555.
- [39] K. Rakstys, S. Paek, P. Gao, P. Gratia, T. Marszalek, G. Grancini, K.T. Cho, K. Genevicius, V. Jankauskas, W. Pisula, M.K. Nazeeruddin, Molecular engineering of face-on oriented dopant free hole transporting material for perovskite solar cells with 19% PCE, *J. Mater. Chem. A* 5 (2017) 7811–7815.
- [40] G. Cotella, J. Baker, D. Worsley, F. De Rossi, C. PleydellPearce, M. Carnie, T. Watson, One-step deposition by slot-die coating of mixed lead halide perovskite for photovoltaic applications, *Sol. Cells* 159 (2017) 362–369.
- [41] F.D. Giacomo, S. Shanmugam, H. Fledderus, B.J. Bruijniers, W.J.H. Verhees, M. S. Dorenkamper, S.C. Veenstra, W. Qiu, R. Gehlhaar, T. Merckx, T. Aernouts, R. Andriessen, Y. Galagan, Up-scalable sheet-to-sheet production of high efficiency perovskite module and solar cells on 6-in. substrate using slot die coating, *Sol. Cells* 181 (2018) 53–59.
- [42] D. Lee, Y.-S. Jung, Y.-J. Heo, S. Lee, K. Hwang, Y.-J. Jeon, J.-E. Kim, J. Park, G. Y. Jung, D.-Y. Kim, Slot-die coated perovskite films using mixed lead precursors for highly reproducible and large-area solar cells, *ACS Appl. Mater. Interfaces* 10 (2018) 16133–16139.
- [43] F. Mathies, T. Abzieher, A. Hochstuhl, K. Glaser, A. Colmann, U.W. Paetzold, G. Hernandez-Sosa, U. Lemmer, A. Quintilla, Multipass inkjet printed planar methylammonium lead iodide perovskite solar cells, *J. Mater. Chem. A* 4 (2016) 19207–19213.
- [44] F. Mathies, H. Eggers, B.S. Richards, G. Hernandez-Sosa, U. Lemmer, U. W. Paetzold, Inkjet-printed triple cation perovskite solar cells, *ACS Appl. Energy Mater.* 1 (2018) 1834–1839.
- [45] Z. Yang, C.-C. Chueh, F. Zuo, J.H. Kim, P.-W. Liang, A.K.-Y. Jen, High-performance fully printable perovskite solar cells via blade-coating technique under the ambient condition, *Adv. Energy Mater.* 5 (2015) 1500328.

- [46] J.H. Kim, S.T. Williams, N. Cho, C.-C. Chueh, A.K.-Y. Jen, Enhanced environmental stability of planar heterojunction perovskite solar cells based on blade-coating, *Adv. Energy Mater.* 5 (2015) 1401229.
- [47] B. Chen, Z.J. Yu, S. Manzoor, S. Wang, W. Weigand, Z. Yu, G. Yang, Z. Ni, X. Dai, Z. C. Holman, J. Huang, Blade-Coated Perovskites on Textured Silicon for 26%-Efficient Monolithic Perovskite/Silicon Tandem Solar Cells, *Joule* 4 (2020) 850–864.
- [48] A.S. Marques, R.M. Faria, J.N. Freitas, A.F. Nogueira, Low-temperature blade-coated perovskite solar cells, *Ind. Eng. Chem. Res.* 60 (2021) 7145–7154.
- [49] S. Chen, X. Xiao, H. Gu, J. Huang, Iodine reduction for reproducible and high-performance perovskite solar cells and modules, *Sci. Adv.* 7 (2021) 8130.
- [50] M. Yang, Z. Li, M.O. Reese, O.G. Reid, D.H. Kim, S. Siol, T.R. Klein, Y. Yan, J. J. Berry, M.F.A.M. van Hest, K. Zhu, Perovskite ink with wide processing window for scalable high-efficiency solar cells, *Nat. Energy* 2 (2017) 17038.
- [51] K. Hwang, Y.-S. Jung, Y.-J. Heo, F.H. Scholes, S.E. Watkins, J. Subbiah, D.J. Jones, D.-Y. Kim, D. Vak, Toward large scale roll-to-roll production of fully printed perovskite solar cells, *Adv. Mater.* 27 (2015) 1241–1247.
- [52] T.M. Schmidt, T.T. Larsen-Olsen, J.E. Carlé, D. Angmo, F.C. Krebs, Upscaling of perovskite solar cells: fully ambient roll processing of flexible perovskite solar cells with printed back electrodes, *Adv. Energy Mater.* 5 (2015) 1500569.
- [53] Z. Wei, K. Yan, H. Chen, Y. Yi, T. Zhang, X. Long, J. Li, L. Zhang, J. Wang, J. Xu, S. Yang, Cost-efficient clamping solar cells using candle soot for hole extraction from ambipolar perovskites, *Energy Environ. Sci.* 7 (2014) 3326–3333.
- [54] K. Yan, Z. Wei, J. Li, H. Chen, Y. Yi, X. Zhang, X. Long, Z. Wang, J. Wang, J. Xu, S. Yang, High-performance graphene-based hole conductor-free perovskite solar cells: schottky junction enhanced hole extraction and electron blocking, *Small* 11 (2015) 2269–2274.
- [55] Z. Yang, C.-C. Cheuh, F. Zuo, J.H. Kim, P.-W. Liang, A.K.-Y. Jen, High-performance fully printable perovskite solar cells via blade-coating technique under the ambient condition, *Adv. Energy Mater.* 5 (2015) 1500328.
- [56] T. Qin, W. Huang, J.-E. Kim, D. Vak, C. Forsyth, C.R. McNeill, Y.-B. Cheng, Amorphous hole-transporting layer in slot-die coated perovskite solar cells, *Nano Energy* 31 (2017) 210–217.
- [57] Y. Liu, Y. Liu, X. Zhan, High-mobility conjugated polymers based on fused-thiophene building blocks, *Macromol. Chem. Phys.* 212 (2011) 428–443.
- [58] R.P. Ortiz, A. Facchetti, T.J. Marks, J. Casado, M.Z. Zgierski, M. Kozaki, V. Hernández, J.T.L. Navarrete, Ambipolar organic field-effect transistors from cross-conjugated aromatic quaterthiophenes; comparisons with quinoidal parent materials, *Adv. Funct. Mater.* 19 (2009) 386–394.
- [59] Z. Fei, X. Gao, J. Smith, P. Pattanasattayavong, E.B. Domingo, N. Stingelin, S. E. Watkins, T.D. Anthopoulos, R.J. Kline, M. Heeney, Near infrared absorbing soluble poly(cyclopenta[2,1-b:3,4-b']dithiophen-4-one)-vinylene polymers exhibiting high hole and electron mobilities in ambient air, *Chem. Mater.* 25 (2013) 59–68.
- [60] M. Zhang, Y. Wang, M. Xu, W. Ma, R. Li, P. Wang, Design of high-efficiency organic dyes for titania solar cells based on the chromophoric core of cyclopentadithiophene-benzothiadiazole, *Energy Environ. Sci.* 6 (2013) 2944–2949.
- [61] M. Saliba, S. Orlandi, T. Matsui, S. Aghazada, M. Cavazzini, J.-P. Correa-Baena, P. Gao, R. Scopelliti, E. Mosconi, K.-H. Dahmen, F. De Angelis, A. Abate, A. Hagfeldt, G. Pozzi, M. Graetzel, M.K. Nazeeruddin, A molecularly engineered hole-transporting material for efficient perovskite solar cells, *Nat. Energy* 1 (2016) 15017.
- [62] Y.-D. Lin, K.-M. Lee, B.-Y. Ke, K.-S. Chen, H.-C. Cheng, W.-J. Lin, S.H. Chang, C.-G. Wu, M.-C. Kuo, H.-C. Chung, C.-C. Chou, H.-Y. Chen, K.-L. Liao, T.J. Chow, S.-S. Sun, Rational design of cyclopenta[2,1-b;3,4-b']dithiophene-bridged hole transporting materials for highly efficient and stable perovskite solar cells, *Energy Technol.* 7 (2019) 307–316.
- [63] Y.-D. Lin, S.Y. Abate, H.-C. Chung, K.-L. Liao, Y.T. Tao, T.J. Chow, S.-S. Sun, Donor–Acceptor–Donor Type Cyclopenta[2,1-b;3,4-b']dithiophene derivatives as a new class of hole transporting materials for highly efficient and stable perovskite solar cells, *ACS Appl. Energy Mater.* 2 (2019) 7070–7082.
- [64] K.-M. Lee, K.S. Chen, J.R. Wu, Y.-D. Lin, S.M. Yu, S.H. Chang, Highly efficient and stable semi-transparent perovskite solar modules with a trilayer anode electrode, *Nanoscale* 10 (2018) 17699–17704.
- [65] Y.-D. Lin, K.-M. Lee, S.H. Chang, T.-Y. Tsai, H.-C. Chung, C.-C. Chou, H.-Y. Chen, T. J. Chow, S.-S. Sun, Molecularly engineered cyclopenta[2,1-b;3,4-b']dithiophene-based hole-transporting materials for high-performance perovskite solar cells with efficiency over 19%, *ACS Appl. Energy Mater.* 4 (2021) 4719–4728.
- [66] K.-M. Lee, C.-H. Lai, W.-C. Chu, S.-H. Chan, Thermal assisted blade coating methylammonium lead iodide films with non-toxic solvent precursors for efficient perovskite solar cells and submodule, *Sol. Energy* 204 (2020) 337–345.
- [67] K.-M. Lee, S.-H. Chan, M.-Y. Hou, W.-C. Chu, S.-H. Chen, S.-M. Yu, M.-C. Wu, Enhanced efficiency and stability of quasi-2D/3D perovskite solar cells by thermal assisted blade coating method, *Chem. Eng. J.* 405 (2021) 126992.
- [68] B. Pal, W.-C. Yen, J.-S. Yang, S.-T. Lin, C.-H. Chuang, C.-Y. Chao, C.-W. Chen, Y.-C. Hun, W.-F. Su, Substituent effect on the optoelectronic properties of alternating fluorene-cyclopentadithiophene copolymers, *Macromolecules* 41 (2008) 6664–6671.
- [69] K. Rakstys, M. Saliba, P. Gao, P. Gratia, E. Kamarasuskas, S. Paek, V. Jankauskas, M. K. Nazeeruddin, Highly efficient perovskite solar cells employing an easily attainable bifluorenylidene-based hole-transporting material, *Angew. Chem., Int. Ed.* 55 (2016) 7464–7468.
- [70] X. Yin, C. Wang, D. Zhao, N. Shrestha, C.R. Grice, L. Guan, Z. Song, C. Chen, C. Li, G. Chi, B. Zhou, J. Yu, Z. Zhang, R.J. Ellingson, J. Zhou, Y. Yan, W. Tang, Binary hole transport materials blending to linearly tune HOMO level for high efficiency and stable perovskite solar cells, *Nano Energy* 51 (2018) 680–687.
- [71] W.-T. Wang, P. Chen, C.-H. Chiang, T.-F. Guo, C.-G. Wu, S.-P. Feng, Synergistic reinforcement of built-in electric fields for highly efficient and stable perovskite photovoltaics, *Adv. Funct. Mater.* 30 (2020) 1909755.
- [72] D. Yang, R. Yang, K. Wang, C. Wu, X. Zhu, J. Feng, X. Ren, G. Fang, S. Priya, S. Liu, High efficiency planar-type perovskite solar cells with negligible hysteresis using EDTA-complexed SnO<sub>2</sub>, *Nat. Commun.* 9 (2018) 3239.
- [73] Z. Bi, X. Rodríguez-Martínez, C. Aranda, E. Pascual-San-José, A.R. Goñi, M. Campoy-Quiles, X. Xu, Defect tolerant perovskite solar cells from blade coated non-toxic solvents, *J. Mater. Chem. A* 6 (2018) 19085–19093.
- [74] S. Wang, Z. Huang, X. Wang, Y. Li, M. Günther, S. Valenzuela, P. Parikh, A. Cabreros, W. Xiong, Y.S. Meng, Unveiling the role of tBP–LiTFSI complexes in perovskite solar cells, *J. Am. Chem. Soc.* 140 (2018) 16720–16730.
- [75] S.N. Habisreutinger, N.K. Noel, H.J. Snaith, R.J. Nicholas, Investigating the role of 4-tert butylpyridine in perovskite solar cells, *Adv. Energy Mater.* 7 (2017) 1601079.
- [76] F. Lamberti, T. Gatti, E. Cescon, R. Sorrentino, A. Rizzo, E. Menna, G. Meneghesso, M. Meneghetti, A. Petrozza, Evidence of spiro-OMeTAD de-doping by tert-butylpyridine additive in hole-transporting layers for perovskite solar cells, *Chem* 5 (2019) 1806–1817.